hydrology

MDPI

Article

Infiltration Assessments on Top of Yungang Grottoes by Time-Lapse Electrical Resistivity Tomography

Deqiang Mao [1,*], Xudong Wang [1], Jian Meng [1], Xinmin Ma [1], Xiaowei Jiang [2], Li Wan [2], Hongbin Yan [3] and Yao Fan [3]

[1] School of Civil Engineering, Shandong University, Jinan 250061, China; 202035047@mail.sdu.edu.cn (X.W.); 201914601@mail.sdu.edu.cn (J.M.); maxmkzx@mail.sdu.edu.cn (X.M.)
[2] School of Water Resources and Environment, China University of Geosciences (Beijing), Beijing 100081, China; jxw@cugb.edu.cn (X.J.); wanli@cugb.edu.cn (L.W.)
[3] Yungang Research Institute, Datong 037034, China; dtyhb@163.com (H.Y.); fanyaosea@163.com (Y.F.)
* Correspondence: maodeqiang@sdu.edu.cn

Abstract: Water plays a vital role in the weathering process of grottoes. Precipitation is a main water source in the grotto hosting mountain rock. In this study, time-lapse electrical resistivity tomography was adopted to track the movement of infiltrated water in a profile in the Yungang Grottoes. Our one-year monitoring data indicated a good resistivity response to rainfall in the shallow unconsolidated soil layers. There were only resistivity decreases in the near surface 5 m across the whole monitoring profile, and resistivity values quickly returned to a neutral state after the rain stopped. Based on the analysis of a typical rainfall event during the rainy season, we found that the infiltrated water cannot continuously move downwards to recharge local groundwater. It moves horizontally to a nearby gully due to the existence of a hydraulic conductive fine sand layer and low permeable mudstone and sandstone base rocks. An artificial infiltration experiment was carried out to further verify the fate of infiltrated water. Based on mass balance analysis, with 10 m^3 of infiltrated water, it only saturated dry soil in the top 1.36 m soil layer on average and this was roughly consistent with our field borehole wetting front verifications at 1.2 and 1.3 m. There were limited horizontal expansions from the infiltrated water. Therefore, based on our monitoring data and analysis, infiltrated water was not the main source of the water involved in the weathering process of the Yungang Grottoes.

Keywords: time-lapse electrical resistivity tomography; Yungang Grottoes; infiltration assessment; rainfall infiltration

Citation: Mao, D.; Wang, X.; Meng, J.; Ma, X.; Jiang, X.; Wan, L.; Yan, H.; Fan, Y. Infiltration Assessments on Top of Yungang Grottoes by Time-Lapse Electrical Resistivity Tomography. *Hydrology* **2022**, *9*, 77. https://doi.org/10.3390/hydrology9050077

Academic Editor: Luca Brocca

Received: 17 March 2022
Accepted: 3 May 2022
Published: 5 May 2022

1. Introduction

Grottoes usually refer to carved shrines built into a rock formation. Many of them are in the World Heritage Sites List [1] and are therefore famous tourist destinations. With their rock body nature, weathering processes create severe threats to the protection of these ancient treasures [2]. Water infiltration or moisture distribution in the rock plays a vital role in the process of grottoes weathering. Rain enters into topsoil layers and flows into fractures and pores of rocks. In the end, it may participate in the water–rock interactions on the grotto's surfaces [3]. Therefore, tracking of water infiltration into the grotto's hosting rock becomes a necessary step to cure the problem.

The ability of soil infiltration can be effectively quantified with existing mature methods, such as the double ring infiltrometer method [4], and its modified version [5]. The movement of infiltrated water can be tracked by directly taking soil samples from different depths and measuring moisture content through oven drying. More advanced methods are also available by neutron probe [6] or by TDR sensors [7]. However, the application of these methods has to disrupt the soil layers by digging open pits or borehole drilling. It is expensive over large areas, and may create potential damages to the precious grottoes. Moreover, it is hard to track the deep infiltration process.

Electrical resistivity tomography (ERT) is advantageous to take large-scale measurements with minimal invasions. Electrical resistivity is highly sensitive to soil property variations. Therefore, it is possible to characterize the subsurface with high resolution. It has been widely used in hydrogeological investigations [8,9]. Advancements in instrumentation have made monitoring of hydrological events possible [10]. By proper experiment designs, various research proved that time-lapse ERT can successfully detect the movement of water in the vadose zone [11,12]. By increasing the fluid salinity, the contrast between the movement of fluid and background porous media can be improved. As demonstrated by several researchers [13,14], time-lapse ERT can track the spatiotemporal evolution of salt plumes in real-time. With the obtained high-resolution images, flow and solute parameters can be therefore inferred [15,16]. So far, there are no ERT monitoring infiltration cases related to the studies of the grotto weathering process.

The Yungang Grottoes are located in the suburbs of Datong city in Shanxi Province, China. In 2001, the site was listed as a World Cultural Heritage Site by UNESCO. For the Yungang Grottoes, all the caves are carved out of sandstone rocks. The studies of their weathering problems have been prioritized since the 1950s [17]. As one of China's largest coal production centers, influences of atmospheric particle depositions within the caves have been heavily studied [18,19]. Due to the lowering of the ground water table by coal mining, condensation water from air humidity by temperature difference has been emphasized [2,20]. However, research regarding the fate of infiltrated water has rarely been carried out [21].

In this study, electrical resistivity measurements were utilized to assess the rainfall infiltration in the Yungang Grottoes. We aimed to see whether the accumulated water could ultimately enter into the grotto caves located at lower locations. First of all, time-lapse ERT monitoring was setup to record subsurface resistivity variations along a profile on top of the grottoes' hosting mountain. At the end of the monitoring period, we further carried out an artificial infiltration test at one segment of the profile to validate the monitored resistivity responses. Soil cores were excavated to provide ground truth of infiltration depth. In the end, we conclude the usefulness of electrical resistivity measurements on infiltration monitoring and assessment. Based on the above information, the paper is organized in four parts. The background provides basic information about the study area. In the methodology, electrical resistivity tomography is explained, and the steps of artificial infiltration test is discussed. The Results and Discussion sections illustrate and analyze the findings from field surveys and infiltration tests. The conclusion shows the usefulness of electrical resistivity measurements on infiltration monitoring and assessment.

2. Background of the Study Area

2.1. Site Background

In the Yungang Grottoes, there are 252 caves and niches housing approximately 51,000 statues within a carved area of 18,000 square meters. Most caves were built in the Northern Wei Dynasty (460–534 AD). Caves deeply extend into rocks along the southern foot of the Wuzhou Mountains. As illustrated in Figure 1, our experiment site was close to the edge of the mountain, and on top of Cave No. 14 to No. 21. The bottom elevation of Cave No. 14 to No.21 was about 1042 m. The elevation of our survey site was roughly 1162 m. There are steep slopes on the north and west sides, and gentle slopes on the east and south sides, which makes the study site a miniature catchment for rainfall runoff. Therefore, the local administrative office is worried about the potential damage of rainfall water infiltration to the grottoes. There are two deep boreholes in the research site (Figure 2). The groundwater levels of boreholes B1 and B2 were 1131 and 1139 m and were stable during our one-year-long study period. Compared to the cave base elevation, the groundwater levels were all below the bottom of the caves.

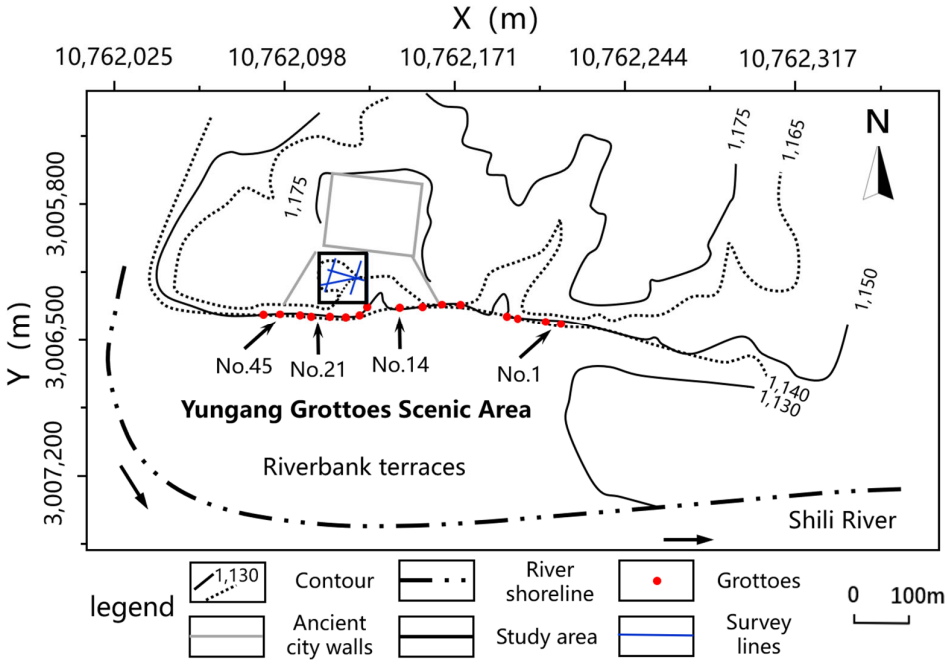

Figure 1. Illustration of Yungang Grottoes and study site. Our study site was between No. 14 and No. 21 caves on top of the grottoes at Wuzhou Mountain. Geophysical survey lines and the infiltration site were all deployed inside the study site. It is marked by the black rectangle. The ERT survey was shown in blue solid lines. Elevation contour lines were shown to depict the topology of the study area.

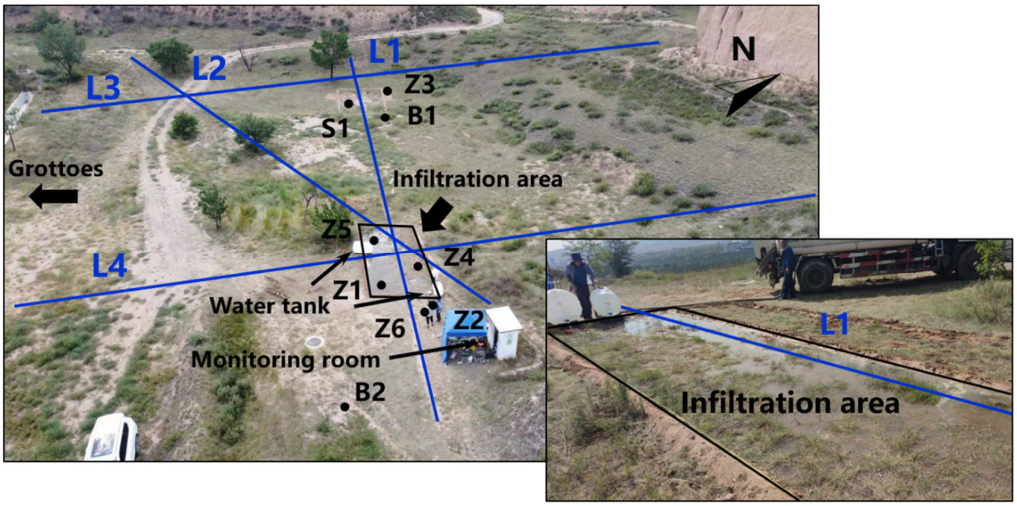

Figure 2. Illustration of survey deployment. There were four resistivity survey lines and L1 served as a long-term monitoring line. Six boreholes Z1 to Z6 were drilled with a manual auger set up to a maximum depth 1.9 m. B1 and B2 were existing deep observation boreholes. The pit at S1 was used for soil and temperature probes. The black rectangle shows the artificial infiltration site.

The Yungang Grottoes are located in semi-arid areas, and the annual precipitation is 372 mm. Over half of the precipitation occurs in the summer period between June and September. The recorded maximum monthly rainfall is about 100 mm. The rainfall data were recorded in a nearby weather station approximately two kilometers from the research site. The lowest average temperature is −10 °C in January, and the highest average temperature is 20 °C in July.

2.2. Geology and Hydrogeology Information

The sculptures were mainly carved into the sandstone of the Jurassic age. This layer of sandstone is covered with two layers of Quaternary sediments on top. As shown by the B1 and B2 borehole profiles depicted in profile L1 of Figure 3, the upper layer is silt and a discontinuous layer of fine sand of 1 to 2.5 m in thickness was below this silt layer. On the research site, this silt layer became thinner towards the mountain edge, ranging from 0.5 to 2 m. There is a layer of mudstone above the Jurassic sandstone layer. The permeability of sandstone rock samples is rather low, ranging from 0.2 to 2.0 md. However, fractures are well developed in the Jurassic sandstone layers, and especially the top of the sandstone layer has gone through the weathering process. The flow of water could be significantly increased because of these fractures.

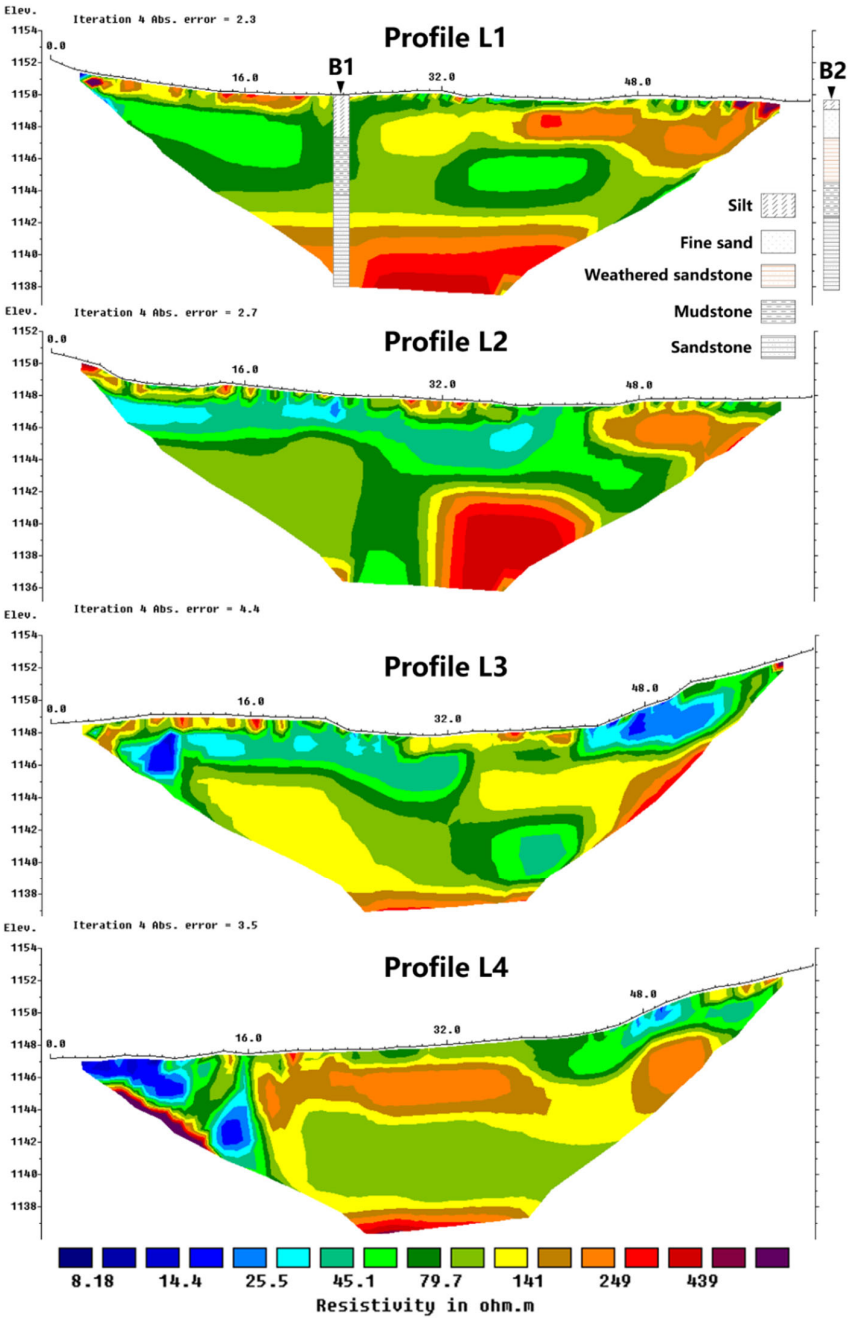

Figure 3. Electrical resistivity results of the four survey lines with surface topography. Borehole B1 and B2 profiles are superposed with profile L1.

3. Methodology

3.1. ERT Method

Both electrical resistivity tomography survey and monitoring methods were adopted in this study. There were in total four resistivity survey lines and one monitoring line deployed (Figure 2). The location of the monitoring line was chosen to align with the existing boreholes B1 and B2, and this line also served as one of the resistivity survey lines. The remaining three lines were deployed to capture the general subsurface heterogeneity information as much as possible. For the resistivity survey, traditional stainless-steel bars were used as electrodes [22]. For the monitoring task, specially manufactured plate electrodes were buried 20 cm below the ground surface. In order to keep low contact resistance to endure long monitoring periods, each electrode was wrapped with saturated bentonite.

There were 32 electrodes on each resistivity profile, and 2 m electrode spacing was adopted. In order to obtain more information in deeper locations, the survey array was optimized based on the Compare R method [23,24]. We used 159 dipole–dipole combinations as the initial survey combinations. During each iteration, five quadrupole combinations were selected from comprehensive measurements based on the resolution by calculating their average model resolution. With 32 electrodes, there were $32 \times 31 \times 30 \times 29/8 = 107{,}880$ non-equivalent electrode combinations. In the end, a much smaller combination was selected to represent the comprehensive set. For the current study, there were 1297 quadrupole combinations in this optimized survey protocol after 24 iterations. Each survey took about 45 min. The survey was conducted in July 2021. For the monitoring function, the data were recorded every eight hours with a self-sustained system powered by solar panels. The data were wirelessly transferred through the internet. Data were processed and inverted on a local computer. Due to power consumption and system requirements, the gradient protocol was used for data monitoring and there were only 294 quadrupole data points for each monitoring task, and it only took about 10 min. ABEM LS2 Terrameter was used for the resistivity measurements and monitoring tasks. Inversion was carried out with Res2DInv using a robust (L1-norm type) method. Time-lapse datasets were inverted simultaneously using a robust smoothness constrain which minimizes the absolute changes in the model resistivity values [25].

In order to better isolate the influence of moisture on the recorded resistivity responses, in situ temperature and moisture probes were installed between the sixth and seventh electrode at three different depths, 10, 30, and 70 cm. Its location is indicated as S1 in Figure 2. The temperature data allowed us to build a simple model used to correct resistivity measurements [26]. All the resistivity results were corrected to resistivity values at 25 °C before taking resistivity ratio calculations.

3.2. Infiltration Test

Based on the survey results, the resistivity variations from the above time-lapse ERT monitoring were further verified with two artificial infiltration tests. Here, we mainly focus on the first test conducted on 8 August 2021. Its exact deployment is shown in Figure 2. A rectangular area was chosen along survey line L1, with the left and right sides located at x = 41 and 50 m. The total surface area was $9 \times 2.5 = 22.5$ m^2. The surrounding earth dams were 15 cm in height. Therefore, the released water was controlled to avoid overflow. The infiltration test lasted for about 2 h. In the end, a total of 10 m^3 of water was poured directly from two storage tanks. The electrical conductivity of the water used for the infiltration test was about 1940 µS/cm. The second test was around the moisture probe S1 (Figure 2). It was performed the next day after the first infiltration test. This location was along a slope on the edge of the study area. This test mainly checked the moisture probe responses during the infiltration event. No resistivity data were collected. In total, 10 m^3 of water was poured during the second test.

When conducting the first infiltration test, electrical resistivity monitoring was conducted to track the water movement. Reference measurements were carried out to obtain a resistivity image of the area under undisturbed conditions. The reference values were

measured one hour before the test. For the infiltration test, we chose to use an optimized array to gain results in high resolution. The surveys were analyzed at five different times. Each repeated resistivity measurement was also inverted using time-lapse inversion, and then the percentage difference relative to the reference model was calculated.

3.3. Borehole Data Analysis

Borehole data are often necessary to aid the interpretation of resistivity inversion results more accurately. Soil samples were taken with a manual auger immediately after the infiltration test. There were six boreholes drilled, i.e., Z1 to Z6, with depths ranging from 1.5 to 1.9 m. Soil samples from three boreholes Z1, Z2, and Z3 were analyzed for grain size distributions. For boreholes Z4, Z5, and Z6, water was added to each borehole to the ground surface. We monitored the hydraulic head decreases inside each borehole. The decreasing trend was used for obtaining relative hydraulic conductivity magnitudes.

4. Results

4.1. ERT Survey

All the measured apparent resistivity data were inverted to obtain resistivity distributions within seven iterations. The RMS were all smaller than 5% which showed the good quality of survey data. Figure 3 gives the resistivity survey results with topography. In general, there is a thin layer of low resistivity on the shallow part. Based on the diagrams of boreholes B1 and B2, it belongs to the silt layer near the ground surface. However, the rather low resistivity (blue color) on the right and left parts of profiles L3 and L4 probably indicates a high percentage of clay content. In all four profiles, there were also relative resistive layers on the near-surface. This is due to the distribution of a discontinuous fine sand layer. This type (yellow or orange color) covers a large part of the right shallow segment of profiles L1 and L2, and most of profile L4. Based on the geological information from B1 and B2 diagrams, the deep rock is sandstone, which is the hosting stratum for grotto carving. It has resistivity values over 100 Ω·m. There is a layer of less resistive mudstone above this sandstone layer, but the thickness is not uniform as indicated by the resistivity results.

4.2. Monitoring Results

The annual soil moisture and resistivity monitoring results are shown in Figure 4. In Figure 4a, the weekly averaged apparent resistivity is shown in the red color. Due to the high contact resistance in winter (8 December 2020 to 4 February 2021) when the soil temperature near the ground surface is below zero degrees, there were no reliable data obtained. A power malfunction also interrupted the monitoring task from 10 July 2021 to 10 August 2021. The overall trend fluctuated from high resistivity in the winter season to low resistivity in the summer season. Precipitation was mainly concentrated in the wet summer season. However, the consistent responses of apparent resistivity to rainfall events were not obvious. As indicated by the moisture probes, there were only small moisture variations at a depth of 10 cm in the whole year. The sudden increase on August 8 was caused by the second infiltration test around S1 at x = 11 m, and it should not be related to any natural rainfall event. The datasets between 6 May and 31 May 2020 were zoomed in to provide more information. As shown in Figure 4b, with detailed daily data, we found that a rainfall event leads to a decrease in the averaged apparent resistivity in the whole profile, such as the rainfall event on 14 and 15 May. This correspondence is especially evident when there is a week-long dry period before a rainfall event. As shown in Figure 4, however, the point moisture data at S1 only showed fluctuations at a depth of 10 cm. It increased from 0.12 to 0.17 cm^3/cm^3. At depths of 30 and 70 cm, the moisture content was almost kept at a constant value of 0.1 cm^3/cm^3.

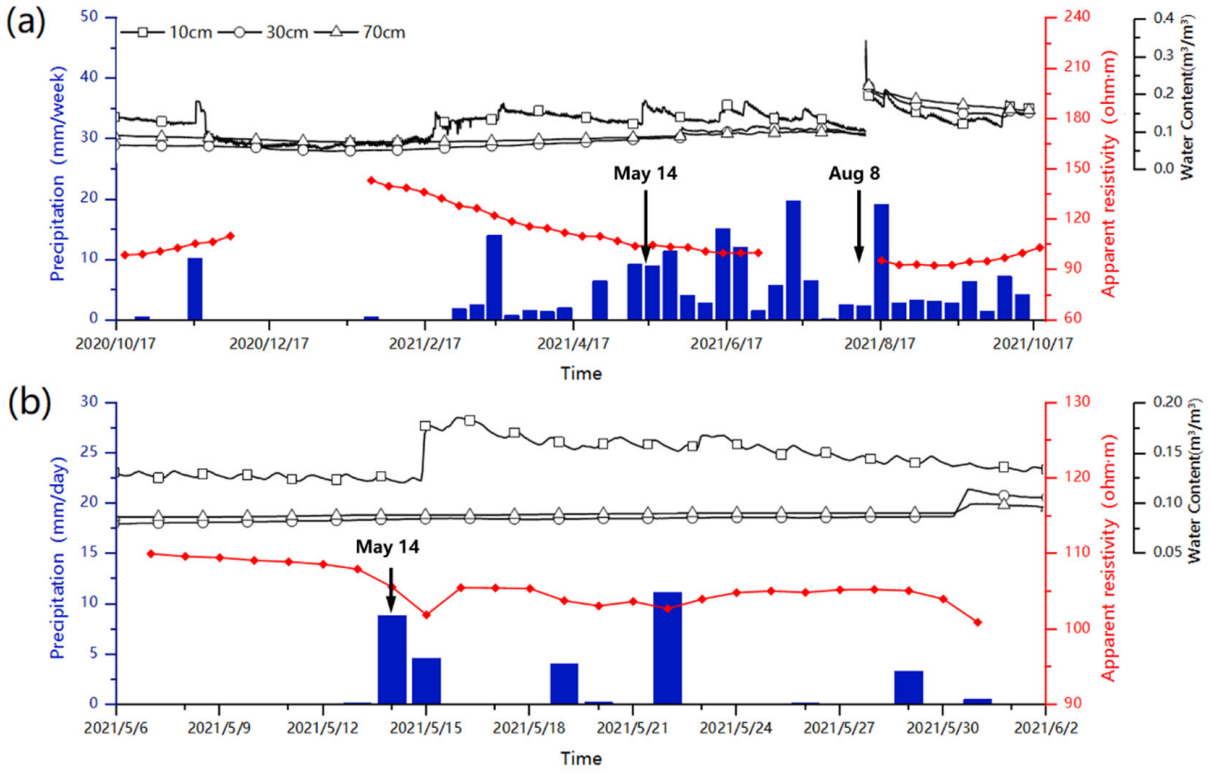

Figure 4. Precipitation, average apparent resistivity, and moisture content data from monitoring line L1. Moisture content data were extracted at three different depths: 10, 30, and 70 cm. (**a**) It shows the annual data variations with weekly average data. (**b**) Data from 6 May to 31 May were used as an example to show the correlations between rainfall events and corresponding resistivity variations.

Next, we focused on the rainfall event from 14 to 15 May. There was in total 18 mm of rainfall in two days. The sequential apparent resistivity data were inverted from 14 May 10:00 to 17 May 2:00. The first dataset was carefully selected to show resistivity distribution before rainfall, and provided a background resistivity with less infiltration impact. The inverted resistivity profiles are shown in the left column of Figure 5, and the resistivity variation percentage with respect to the first profile are shown in the right column. From the resistivity variations, we can see there was a significant resistivity drop across the whole profile in areas less than 5 m [27]. On the left part, it looks like there was a preferential flow channel extending to deeper locations where it indicates a decreased resistivity from x = 10 to 20 m. After the rainfall stopped on 15 May at 9:00, the resistivity variation bounced back to normal on 16 May at 2:00. As time went on, the decreased resistivity region still occupied the near-surface areas, but most areas in the profile had already started going back to a neutral state, i.e., resistivity variation percentage equaled zero. There was still a sign of decreased resistivity due to the potential preferential flow path on the left of each profile, but it was less evident.

As mentioned above, the moisture probe located at S1 only had a subtle increase at a depth of 10 cm, and its projected location along profile L1 is shown with arrows in Figure 5. The moisture content responses in general fit the resistivity variations. We did not expect a perfect fit between the point probe data and pixel variations along the profiles. Moreover, the monitoring profile L1 went through the excavation pit which buried the moisture probes. Therefore, the profile measured the resistivity responses of disturbed and loosed soils. It was slightly different from the rest of the profiles.

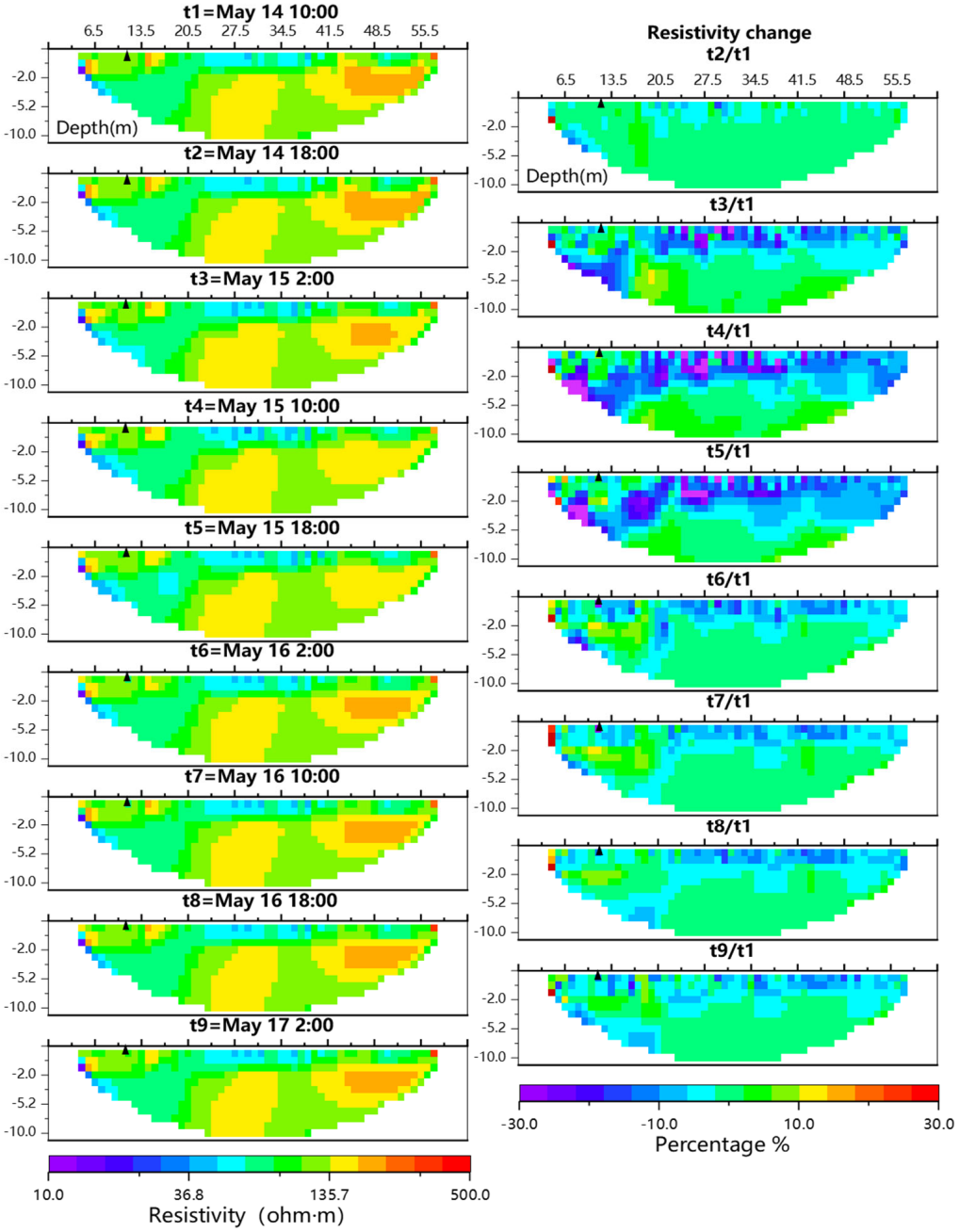

Figure 5. An example of time-lapse resistivity profiles from 14 to 17 May. The depth axis is exaggerated for better illustration. The left column shows the inverted resistivity profiles at nine different times with eight-hour intervals. On the right column, it shows the resistivity variation percentages with respect to the first profile on 14 April at 10:00 in the first column. The arrow marks the soil moisture probe location S1 at x = 11 m.

4.3. Time-Lapse Monitoring of Artificial Infiltration Test

The resistivity variations in profile L1 during the artificial infiltration test are shown in Figure 6. The monitored resistivity results are shown in the left column of Figure 6, and the resistivity variations are shown in the right column. The scope of the infiltration pond is constrained with two arrows at x = 41 and x = 50 m on the right in each figure. The arrow on the left-hand side at x = 11 m represents the location of the moisture content probe. As for the first resistivity variation percentage t2/t1, there was already a weak resistivity decrease. This was because before the start of the first infiltration test, a trial test was initiated to test the configuration of the infiltration test and this decrease was a sign of this trial test.

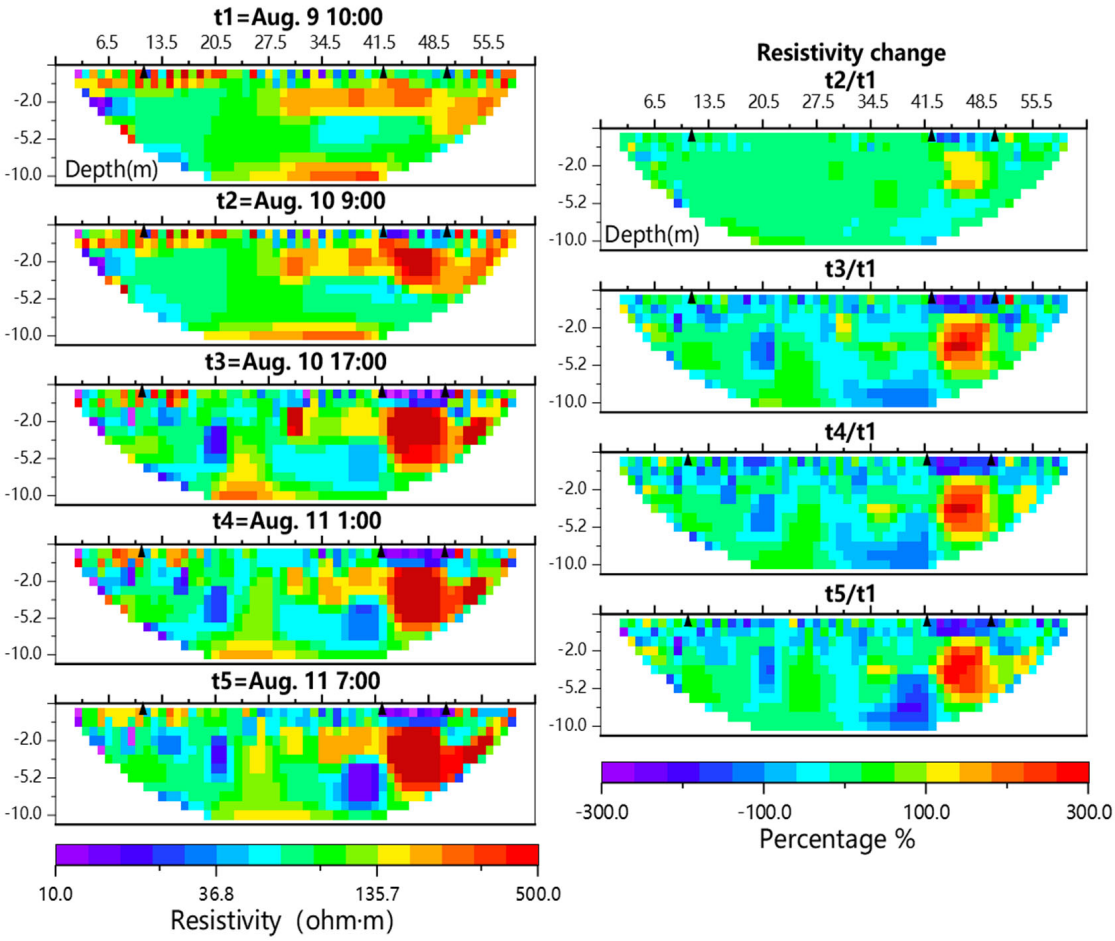

Figure 6. Time-lapse resistivity profiles during the infiltration tests. The depth axis is zoomed in for better illustration. The left column shows the inverted resistivity profiles at five different times. On the right column, it shows the resistivity variations with respect to the resistivity result from the first profile on 9 August at 10:00 in the left column. The arrows mark the soil moisture probe at x = 11 m on the left side and infiltration site location on the right side.

After the end of the first infiltration test on 10 August at 16:00, we took a resistivity survey at t3 = 17:00. For all the monitoring results thereafter, there is a thin layer of decreased resistivity marked by a purple color close to the surface corresponding to the infiltration of water. However, there was an abnormally increased resistivity right below this thin layer between x = 42 and 50 m. There was also a resistivity decrease area below this abnormal high resistivity region. This abnormal increase or decrease in resistivity was due to the relatively large electrode spacing compared to the thin layer of water infiltration [28]. It is not a true reflection of the infiltration process. Other than these variations close to the infiltration site, the rest of the domain showed resistivity changes as well. However, we believe these variations were mainly caused by the noises during our field survey. Even though these areas showed a sign of resistivity decrease, there was no water accumulated on the ground surface at all or hydraulic connections to the infiltration area. For this kind of monitoring, we may need to add more geophysical monitoring methods to reduce uncertainty and help data interpretation, such as induced polarization monitoring which is insensitive to salinity and less sensitive to moisture content variations [10].

4.4. Borehole Data Verification

After the infiltration test, three boreholes were excavated with a manual auger. The field falling head experiment results from boreholes Z4, Z5, and Z6 are shown in Figure 7. Since they were open boreholes, water will dissipate from the whole borehole. The infil-

tration areas shrink with the decrease in the water table inside the borehole. It was hard to attain an analytical solution for this transient process [29]. Therefore, only the speed of the decreasing head was compared. Based on the open-pit falling head experiment and the head decrease trend in the three boreholes [30], a steeper slope of the head decrease trend around the soils in Z6 indicated a relatively larger hydraulic conductivity than soils around Z4 and Z5. Based on field inspections of soil samples, the infiltration front reaches 1.3 m in Z4, and 1.2 m in Z5. This slight difference was also consistent with the slightly steeper hydraulic head drop in Z4 than Z5. Grain size distribution results from boreholes Z1, Z2, and Z3 are shown in Figure 8. Since the total amount of grains larger than 75 µm was less than 50%, the soil samples were all categorized as silt. This result was consistent with B1 and B2 diagrams as shown in Figure 3. Based on all the 15 samples in the shallow 2 m depth, their grain size distributions almost followed the same trend. This indicates the homogeneity of the near-surface soil. Therefore, the subtle grain size differences can create minor hydraulic variations as indicated by the artificial infiltration test and borehole infiltration falling head experiment. This further indicated the representation of the survey results from the current study.

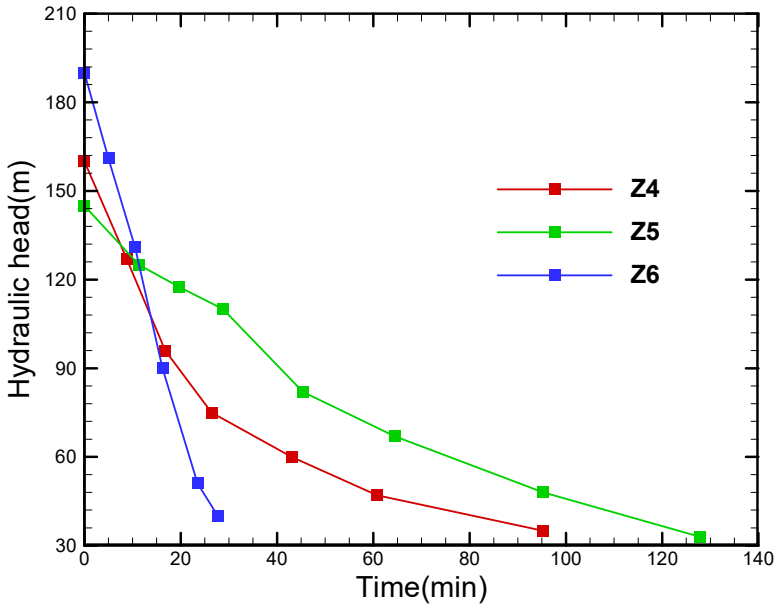

Figure 7. Decrease in hydraulic heads from falling head experiments in three open boreholes Z4, Z5, and Z6 in the artificial infiltration site.

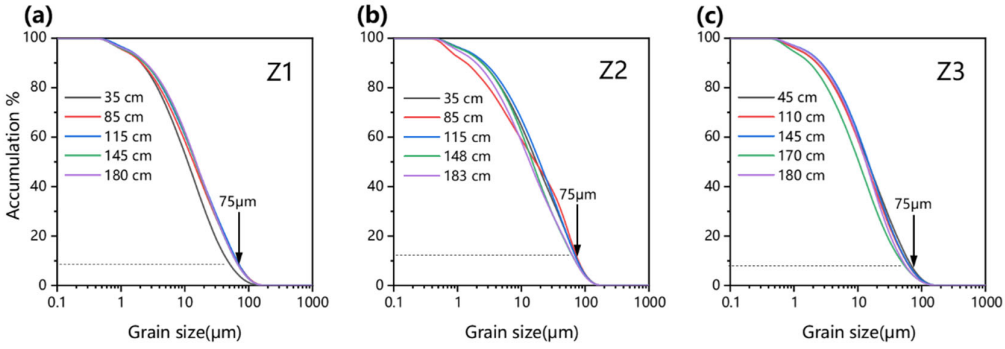

Figure 8. Grain size distributions (GSD) of the soil sample from boreholes. The dashed line shows the percentage corresponding to the grain size at 75 µm. (**a**) GSD for borehole Z1, (**b**) GSD for borehole Z2, (**c**) GSD for borehole Z3. The dashed line shows the percentage corresponding to the grain size at 75 µm.

5. Discussion

As seen from the resistivity ratios of the infiltration test, the maximum penetration was roughly 1.2 m and this depth was also validated from the excavation of boreholes Z4 and Z5. Below this depth, only dry soil samples were found. The porosity of soil samples from these two boreholes has an average value 0.43 [21]. A field water content of 0.10 cm^3/cm^3 below our infiltration site was seen from moisture probe data in S1. If we assumed that lateral flow could be neglected, all the infiltrated water advanced vertically. With a total amount of 10 m^3 of water infiltration and 22.5 m^2 of the infiltration area, the depth of infiltration can be calculated $10/(22.5 \times 0.33) = 1.35$ m. It roughly equals our field excavation depths of 1.2 and 1.3 m. Therefore, the 10 m^3 water was all consumed for soil saturation rather than moving further downwards. However, due to the limited amount of water infiltration in our experiments, the infiltration front does not go deeper as shown by field monitoring results (e.g., Figure 5). We also need to emphasize here that observation data taken in two-dimensional and electrode spacing was assigned at 2 m. Infiltrated water moved in both downwards and horizontal directions. These details can be retrieved with three-dimensional monitoring work and smaller electrode spacings. Our current setup can only capture the general trend of the infiltration process.

With results from our artificial infiltration test and as observed during the one-year-long field test, water can indeed quickly enter the subsurface. On the other hand, based on the topography of the study areas, it became a small catchment, and this phenomenon further raised concerns about the rainfall infiltration problems on top of the Yungang Grottoes' hosting mountain. Indeed, it drives the resistivity monitoring task of this study. Where does infiltrated water go? Based on our annual field resistivity monitoring data, the resistivity decrease region shrinks quickly after the stop of rainfall events, and decreased resistivity only stays in areas close to the ground surface (right column of Figure 5, after time t6). The resistivity variation percentages around depths 2 to 5 m quickly returned to zero. The borehole profile of B2 indicated a layer of fine sand from 2 to 6 m. Based on the resistivity survey results, this fine sand layer was well distributed around this artificial infiltration test site. The high hydraulic conductivity could quickly dissipate the infiltrated water. However, there were no resistivity variations in deeper locations, such as the intermediate mudstone layer and sandstone base rock. Considering the low permeable nature of mudstone and sandstone, the infiltrated water can only move laterally rather than moving further downwards. Moreover, on the east of borehole B2, there is a gully which is not shown in Figure 2, where water can move freely in a downhill direction. Therefore, based on the monitored resistivity data in a whole year period and infiltration test, we believe the rainfall can infiltrate the subsurface quickly, but most infiltrated water dissipates horizontally and discharges back to the surface again. The rainfall water can hardly go deep in the grottoes' hosting mountain, and therefore does not threaten the statues carved in the sandstone. Moreover, according to the topography of the research site, the ground surface can be paved for easy runoff production. This can further reduce the amount of infiltration which in turn protects the safety of the grottoes.

In the end, we would like to mention that our long-term monitoring survey was only carried out at one profile and the artificial infiltration test was quantitative, with a small infiltration perturbation. Here we are trying to illustrate the usage of the ERT method for site characterization and infiltration monitoring. Three-dimensional coverage and more hydraulic tests are needed to give more accurate results.

6. Conclusions

In this study, we conducted a long-term resistivity monitoring task in a profile on top of the Yungang Grottoes' hosting mountain. We aimed to test the density of the rainfall water for grotto protection. Our results prove that time-lapse electrical resistivity tomography can be a useful tool to track the moving infiltration front. The following major conclusions and future developments based on the current findings can be made from our research.

The one-year-long resistivity monitoring shows rainfall water can infiltrate into a maximum depth of about 5 m, and the quick dissipation in depths of around 2 to 5 m is caused by a layer of fine sand. Our field infiltration test further proves the advantage of resistivity monitoring function. But our existing 2 m spacing creates several artifacts in the resistivity profile. Future similar experiments should consider smaller electrode spacings to characterize thin layer moisture dynamic distribution, and the test site should be better placed in the central part of the resistivity line. If possible, dense three-dimensional resistivity lines can be deployed to capture the overall shape of the infiltration front.

Based on the topography of the field site, the infiltrated water does not go further into the sandstone layer where the carved statues stand, and it quickly discharges in the gully areas. Therefore, based on our field monitoring data and analysis, the rainfall infiltration is not the main source of the water formed on the surface of the Yungang Grottoes statues.

Author Contributions: Conceptualization: D.M.; methodology: D.M., X.W. and L.W.; formal analysis: X.W. and J.M.; data curation: X.J., H.Y., Y.F., X.M., X.W. and J.M.; writing: D.M. and X.W.; review and editing: X.W. All authors have read and agreed to the published version of the manuscript.

Funding: This research was funded by the National Key R&D Program of China, grant number 2019YFC1520500, and Shandong National Science Foundation, grant number ZR2019MEE109. The work is also supported by Shanxi Cultural Relics Bureau through contract numbers 208141400241 and 208141400237.

Conflicts of Interest: The authors declare no conflict of interest.

References

1. UNESCO. World Heritage List (Ordered by Year). Available online: https://whc.unesco.org/en/list/&order=year (accessed on 26 May 2020).
2. Guo, F.; Jiang, G. Investigation into rock moisture and salinity regimes: Implications of sandstone weathering in Yungang Grottoes, China. *Carbonates Evaporites* **2015**, *30*, 1–11. [CrossRef]
3. Liu, B.; Peng, W.; Li, H.; Qu, J. Increase of moisture content in Mogao Grottoes from artificial sources based on numerical simulations. *J. Cult. Herit.* **2020**, *45*, 135–141. [CrossRef]
4. Singer, M.J.; Blackard, J. Slope angle-interrill soil loss relationships for slopes up to 50%. *Soil Sci. Soc. Am. J.* **1982**, *46*, 1270–1273. [CrossRef]
5. Lili, M.; Bralts, V.F.; Yinghua, P.; Han, L.; Tingwu, L. Methods for measuring soil infiltration: State of the art. *Int. J. Agric. Biol. Eng.* **2008**, *1*, 22–30.
6. Kodikara, J.; Rajeev, P.; Chan, D.; Gallage, C. Soil moisture monitoring at the field scale using neutron probe. *Can. Geotech. J.* **2014**, *51*, 332–345. [CrossRef]
7. He, H.; Turner, N.C.; Aogu, K.; Dyck, M.; Feng, H.; Si, B.; Wang, J.; Lv, J. Time and frequency domain reflectometry for the measurement of tree stem water content: A review, evaluation, and future perspectives. *Agric. For. Meteorol.* **2021**, *306*, 108442. [CrossRef]
8. Binley, A.; Kemna, A. DC resistivity and induced polarization methods. In *Hydrogeophysics*; Springer: Berlin/Heidelberg, Germany, 2005; pp. 129–156.
9. Revil, A.; Karaoulis, M.; Johnson, T.; Kemna, A. Some low-frequency electrical methods for subsurface characterization and monitoring in hydrogeology. *Hydrogeol. J.* **2012**, *20*, 617–658. [CrossRef]
10. Weigand, M.; Zimmermann, E.; Michels, V.; Huisman, J.A.; Kemna, A. Design and operation of a long-term monitoring system for spectral electrical impedance tomography (sEIT). *Geosci. Instrum. Methods Data Syst. Discuss.* **2022**, 1–35.
11. Deiana, R.; Cassiani, G.; Kemna, A.; Villa, A.; Bruno, V.; Bagliani, A. An experiment of non-invasive characterization of the vadose zone via water injection and cross-hole time-lapse geophysical monitoring. *Near Surf. Geophys.* **2007**, *5*, 183–194. [CrossRef]
12. Looms, M.C.; Jensen, K.H.; Binley, A.; Nielsen, L. Monitoring unsaturated flow and transport using cross-borehole geophysical methods. *Vadose Zone J.* **2008**, *7*, 227–237. [CrossRef]
13. Slater, L.; Binley, A.; Daily, W.; Johnson, R. Cross-hole electrical imaging of a controlled saline tracer injection. *J. Appl. Geophys.* **2000**, *44*, 85–102. [CrossRef]
14. Kemna, A.; Vanderborght, J.; Kulessa, B.; Vereecken, H. Imaging and characterisation of subsurface solute transport using electrical resistivity tomography (ERT) and equivalent transport models. *J. Hydrol.* **2002**, *267*, 125–146. [CrossRef]
15. Koestel, J.; Vanderborght, J.; Javaux, M.; Kemna, A.; Binley, A.; Vereecken, H. Noninvasive 3-D transport characterization in a sandy soil using ERT: 1. Investigating the validity of ERT-derived transport parameters. *Vadose Zone J.* **2009**, *8*, 711–722. [CrossRef]
16. Koestel, J.; Vanderborght, J.; Javaux, M.; Kemna, A.; Binley, A.; Vereecken, H. Noninvasive 3-D transport characterization in a sandy soil using ERT: 2. Transport process inference. *Vadose Zone J.* **2009**, *8*, 723–734. [CrossRef]

17. Huang, J.; Wan, L.; Peng, T.; Cao, W.; Wang, X. Exploration project of water source and some achievements in Yungang Grottoes. *Eng. Investig.* **2012**, *40*, 1–5. (In Chinese)
18. Christoforou, C.S.; Salmon, L.G.; Cass, G.R. Air exchange within the Buddhist cave temples at Yungang, China. *Atmos. Environ.* **1996**, *30*, 3995–4006. [CrossRef]
19. Liu, R.Z.; Zhang, B.J.; Zhang, H.; Shi, M.F. Deterioration of Yungang Grottoes: Diagnosis and research. *J. Cult. Herit.* **2011**, *12*, 494–499. [CrossRef]
20. Wang, X.-S.; Wan, L.; Huang, J.; Cao, W.; Xu, F.; Dong, P. Variable temperature and moisture conditions in Yungang Grottoes, China, and their impacts on ancient sculptures. *Environ. Earth Sci.* **2014**, *72*, 3079–3088. [CrossRef]
21. Wang, X.; Wan, L.; Peng, T.; Dong, P.; Qian, J. Formation and Migration of Infiltration Water in Yungang Grottoes. *Eng. Investig.* **2021**, *11*, 12–16. (In Chinese)
22. LaBrecque, D.; Daily, W. Assessment of measurement errors for galvanic-resistivity electrodes of different composition. *Geophysics* **2008**, *73*, 55–64. [CrossRef]
23. Wilkinson, P.B.; Loke, M.H.; Meldrum, P.I.; Chambers, J.E.; Kuras, O.; Gunn, D.A.; Ogilvy, R.D. Practical aspects of applied optimized survey design for electrical resistivity tomography. *Geophys. J. Int.* **2012**, *189*, 428–440. [CrossRef]
24. Loke, M.; Wilkinson, P.; Uhlemann, S.; Chambers, J.; Oxby, L. Computation of optimized arrays for 3-D electrical imaging surveys. *Geophys. J. Int.* **2014**, *199*, 1751–1764. [CrossRef]
25. Loke, M. Time-Lapse resistivity imaging inversion. In Proceedings of the EEGS-ES 1999, Budapest, Hungary, 6–9 September 1999; p. 1.
26. Chambers, J.; Gunn, D.; Wilkinson, P.; Meldrum, P.; Haslam, E.; Holyoake, S.; Kirkham, M.; Kuras, O.; Merritt, A.; Wragg, J. 4D electrical resistivity tomography monitoring of soil moisture dynamics in an operational railway embankment. *Near Surf. Geophys.* **2014**, *12*, 61–72. [CrossRef]
27. Descloitres, M.; Ruiz, L.; Sekhar, M.; Legchenko, A.; Braun, J.-J.; Mohan Kumar, M.; Subramanian, S. Characterization of seasonal local recharge using electrical resistivity tomography and magnetic resonance sounding. *Hydrol. Process.* **2008**, *22*, 384–394. [CrossRef]
28. Clément, R.; Descloitres, M.; Günther, T.; Ribolzi, O.; Legchenko, A. Influence of shallow infiltration on time-lapse ERT: Experience of advanced interpretation. *C. R. Geosci.* **2009**, *341*, 886–898. [CrossRef]
29. Reynolds, W.D. Measuring Soil Hydraulic Properties Using a Cased Borehole Permeameter: Steady Flow Analyses. *Vadose Zone J.* **2010**, *9*, 637–652. [CrossRef]
30. Rodgers, M.; Mulqueen, J. Field-saturated hydraulic conductivity of soils from laboratory constant-head well tests. *Irrig. Drain. Syst.* **2004**, *18*, 315–327. [CrossRef]